Magmatic underplating and crustal intrusions accommodate extension during Red Sea continental rifting

Alessio Sanfilippo, Marco Ligi, Riccardo Avanzinelli, Valentin Basch, Alessandro Bragagni, Alessandro Decarlis, Hervé Guillou, Sébastien Nomade, Najeeb Rasul, Luigi Vigliotti, et al.

nature communications

Article

https://doi.org/10.1038/s41467-025-61598-0

Magmatic underplating and crustal intrusions accommodate extension during Red Sea continental rifting

Received: 20 November 2024

Accepted: 26 June 2025

Published online: 14 July 2025

Check for updates

Alessio Sanfilippo[1,2], Marco Ligi[3] ✉, Riccardo Avanzinelli[4], Valentin Basch[1,2], Alessandro Bragagni[3,4], Alessandro Decarlis[5], Hervé Guillou[6], Sébastien Nomade[6], Najeeb Rasul[7], Luigi Vigliotti[3] & Sandro Conticelli[4,8]

Magmatism's role in continental rupture and ocean formation remains a critical question in Earth Sciences. The Red Sea, where Arabia is rifting from Nubia, offers an ideal setting to explore this process. This study analyses geochemical and isotopic data from gabbros and basaltic dikes in the Tihama Asir complex, formed during early Red Sea rifting (Late Oligocene). The results show that asthenospheric melts assimilated ancient lower crust before rising into shallow magma chambers with minimal upper crustal contamination. Rising asthenosphere driven by the Afar plume and by extensional stresses thermally weakened the lower crust, allowing it to decouple from the mantle, causing depth-dependent deformation. The generated asthenospheric melts underplated and intruded the thinning continental crust protracting continental rifting by re-thickening of the crust and accommodating extension. This study provides the evidence of tholeiitic underplating beneath thick continental crust during early rifting, substantially postponing the onset of seafloor spreading.

Over billions of years, the Earth's internal processes cyclically formed and broke apart supercontinents, leading to the birth of new oceans. The Wilson Cycle explains how continents split, forming passive margins[1,2]. Continental fragmentation takes place due to extensional stress, initiating rifts where the lithosphere is affected by progressive mechanical deformation and magmatic processes. This process continues until the continental lithosphere ultimately fractures, creating new oceanic lithosphere that separates two conjugate juvenile continental margins. The East African Rift System, including the Red Sea, represents various stages of this process, from continental rifts to an emerging ocean. This rift system began fragmenting the Afro-Arabian shield since the late Oligocene, influenced by a mantle plume impacting the Afar region around 34 Ma[3–5]. Magnetic anomalies in the Red Sea suggest an ongoing formation of oceanic crust, with the southern region reaching further in this process than the central or northern regions[6–8]. Variations in the amount of extension may reflect different stages of the rifting process, while differences in GNSS-derived relative velocities between the Arabian and Nubian plates, increasing from ~7 mm/yr in the northern Red Sea to ~16 mm/yr in the southern Red Sea[9] suggest distinct dominant mechanisms for the formation of the northern and southern Red Sea. The onset of rifting in the Red Sea was preceded by flood basalts erupted in Ethiopia, NE

[1]Dipartimento di Scienze della Terra e dell'Ambiente, Università di Pavia, Via Ferrata 1, 27100 Pavia, Italy. [2]Istituto di Geoscienze e Georisorse, CNR, Via Ferrata 1, 27100 Pavia, Italy. [3]Istituto di Scienze Marine, CNR, Via Gobetti 101, 40129 Bologna, Italy. [4]Dipartimento di Scienze della Terra, Università di Firenze, Via La Pira, 4, 50121 Firenze, Italy. [5]Dipartimento di Fisica e Geologia, Università degli Studi di Perugia, Piazza Università 1, 06123 Perugia, Italy. [6]Laboratoire de Sciences du Climat et de l'Environnement, CEA, UMR 8212, UVSQ, IPSL and Université de Paris-Saclay, Gif-sur-Yvette, France. [7]Geological and Geophysical Research Systems, Toronto, Canada. [8]Istituto di Geologia Ambientale e Geoingegneria, CNR, Strada Provinciale 35d, 00010 Montelibretti (RM), Italy. ✉e-mail: marco.ligi@bo.ismar.cnr.it

Sudan, and SW Yemen[5], also associated with rhyolitic volcanism[10,11]. Abundant melt was injected into the Arabian basement in the early stages of rifting (26–21 Ma)[5,12–15] as testified by the occurrence of thousands of kilometers-long dike swarms running NW-SE parallel to the Arabian coast of the Red Sea[12,16], along with the contemporaneous Tihama Asir[12] (southern Red Sea), Al Lith[16] (central Red Sea), and Quseir[13,14] (northern Red Sea) magmatic complexes, which include gabbros, basaltic dikes, and granophyres. Widespread gabbro and dike injection was followed by successive phases of volcanism, leading to the formation of extensive alkali-basalt lava fields (harrats). Some of these phases had finite eruption periods, while others began at different times and continued into recent history[12,16–20] (Fig. 1).

The formation of a magma-rich margin during rifting is driven by multiple geological factors[21,22]. A key factor is the magmatic supply, where sufficient magma generation from the mantle is essential for processes like dike injection and underplating (i.e., addition of mafic magma to the lower crust and uppermost mantle around the Moho in the form of batholiths and sill-like structures[23]). Efficient heat transfer from the mantle can promote localized melting and assimilation of crustal material, affecting the formation of transitional crust. The composition and thickness of the pre-existing continental crust affect how it interacts with ascending magmas, while the rheological properties of the lithosphere, such as its strength and viscosity, impact deformation behavior. The duration of rifting, the divergence rate and magmatic activity also play a critical role[24]. Understanding these constraints is fundamental for modeling magma-rich margin formation and predicting their evolution.

The Tihama Asir magmatic complex in southernmost Saudi Arabia serves as a key location to study the initial phase of syn-rift magmatism and its influence on the geodynamic evolution of the southern Red Sea rift system (Fig. 1), and, more broadly, of magma-rich rift systems. This region provides insights into the interplay between magmatic supply, tectonic setting, heat transfer, and crustal composition during the early stages of rifting[12]. In this study, we present geochemical data including bulk rock major and trace elements, as well as Sr, Nd, and Pb isotopic compositions of the Tihama Asir gabbros and dykes, in order to investigate the magma source and its migration and emplacement within the crust during rifting. We also measured the magnetic properties of these rocks to better constrain the geophysical signals they produce. Additionally, $^{40}Ar/^{39}Ar$ age determinations, combined with existing geophysical data, enable us to reconstruct the evolution of the magmatic complex within the broader framework of Red Sea rifting and ocean basin development.

Results

The Tihama Asir igneous complex

The Tihama Asir magmatic complex is located east of the Jizan coastal plain in southwestern Saudi Arabia (Fig. 1). It consists of various layered gabbroic bodies with compositional layering ranging from relatively primitive olivine gabbros to more evolved lithologies such as oxide gabbros, with layering occurring at meter- to decameter-scale and tending to diminish up-section, akin to typical Penrose-type ophiolite stratigraphy[25–27]. The gabbros are in primary contact with granophyre granitic intrusions, with preserved intrusive contacts to the strongly faulted Arabian Shield Neoproterozoic basement comprising Pan-African granitoids, low-grade metamorphic rocks, and gneisses[26]. Diffuse basaltic to rhyolitic dike swarms locally overlay the gabbroic lithologies and intrude the continental basement[12,26,27]. Our $^{40}Ar/^{39}Ar$

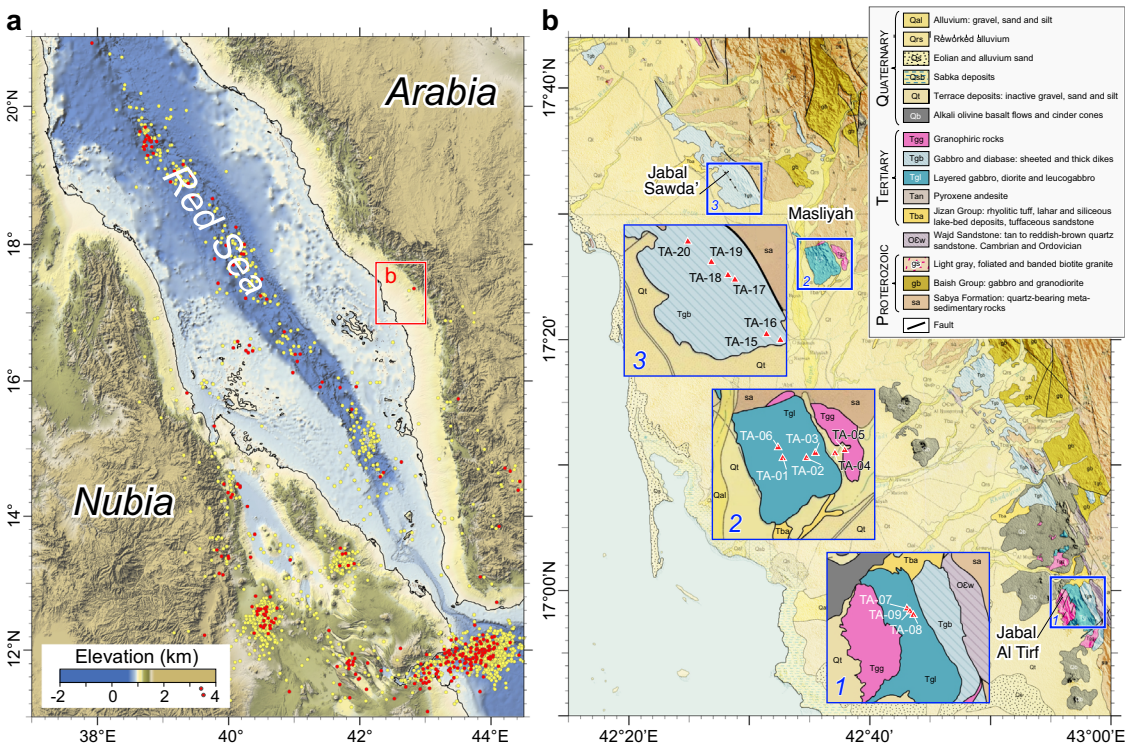

Fig. 1 | The southern Red Sea and the Tihama Asir magmatic complex. **a** Topography and main morphotectonic features of the southern Red Sea region derived from a combination of elevation and bathymetry data sourced from the SRTM30[85] and GEBCO_2024 (GEBCO Compilation Group, doi:10.5285/1c44ce99-0a0d-5f4f-e063-7086abc0ea0f) global grids, respectively. Yellow and red dots, earthquake epicenters with momentum magnitude $3 < M_w < 4$ and $M_w > 4$, respectively, since 1976 from the International Seismological Data Center. The labeled red box refers to the Tihama Asir area displayed in (**b**). **b** Geological map of the Tihama Asir area based on structural and geological data from refs. 26,27,86. The labeled blue boxes correspond to details of the Tihama Asir magmatic complex shown in the insets, indicating sample locations from the Jabal al Tirf (inset 1) and Masliyah (inset 2) plutons, as well as from the sheeted dikes of Jabal Sawdah (inset 3). Mercator projection at 17°N, datum WGS84; sun illumination from NW. Spatial analysis and mapping are performed using the PLOTMAP software[87].

https://doi.org/10.1038/s41467-025-61598-0

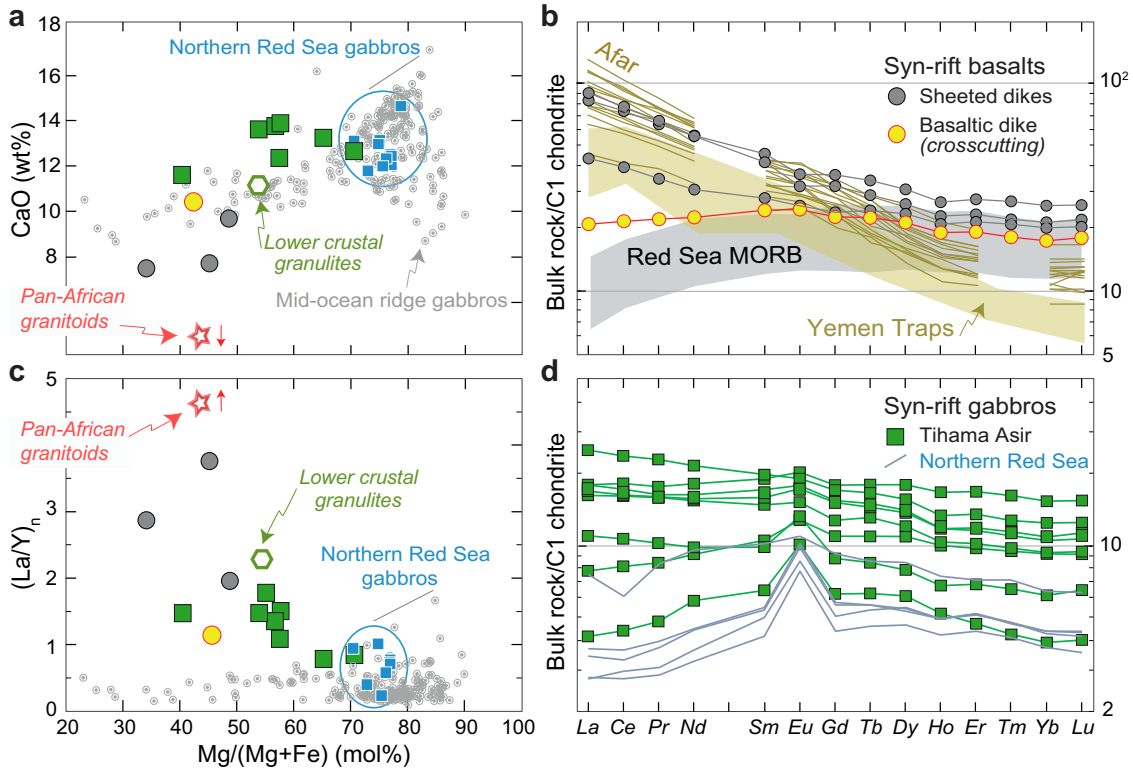

Fig. 2 | Bulk rock major and trace element compositions of intrusive and extrusive rocks of Tihama Asir magmatic complex (Supplementary Data S2). **a** CaO (wt%) versus Mg# (Mg/[Mg + Fe] × 100; mol%). The yellow-filled circle indicates the composition of sample TA-02/Dy-1, taken from a basaltic dike that crosscuts the layered gabbros. **b** $(La/Y)_n$ ratios normalized to chondrite[88] versus Mg#. The average compositions of lower crustal granulites and Pan-African granitoids are from refs. 42,45. Additionally, syn-rift gabbros from the northern Red Sea[14] and gabbros from the Mid-Atlantic Ridge[89] are plotted, which display low and constant $(La/Y)_n$ ratios compared to the Tihama Asir gabbros. **c** Chondrite-normalized REE patterns of extrusives and **d** of intrusives from the southern Red Sea, including syn-rift basalts (this study), Afar basalts[43], Yemen trap[41,42], and present-day Red Sea MORB[32–34].

age determination of 26.03 ± 0.54 Ma and recalibrated previous $^{40}Ar/^{39}Ar$ datings[28] of the Tihama Asir intrusive rocks and the dike swarms constrain their age to within the range 26–21 Ma (Supplementary Fig. S1; Supplementary Data S1). Faulting in this area is suggested to have begun around 29 Ma[15], just a few million years prior to the formation of the magmatic complex. This temporal relationship implies that the Tihama Asir magmatic complex formed due to extensive magmatism during the early stages of Red Sea continental rifting[12,27–29].

Petrology and geochemistry

The most primitive Tihama Asir olivine gabbros show petrological and geochemical characteristics consistent with formation from tholeiitic parental melts, resembling modern MORBs (Supplementary Data S2). However, the evolved gabbros and oxide gabbros show saturation of phlogopite and selective enrichments in LREE and highly incompatible elements (Rb, Ba, U, Th, Nb, Sr, K). The geochemical evolution of the parental melts diverged progressively from that of oceanic tholeiites, suggesting a gradual assimilation of continental crust during the emplacement of the gabbroic bodies (Fig. 2). Similarly, the dike swarms overlying the gabbros (sheeted dike complex) exhibit transitional affinity, with selective enrichments in LREE and highly incompatible elements compared to Red Sea MORB and sub-chondritic Nb-Ta/LREE ratios. These dikes are in chemical equilibrium with the clinopyroxene in the gabbros and are interpreted as melts extracted from hybridized gabbroic crystal mush after high degrees of contamination from upper crustal material.

Furthermore, meter-scale anastomosed basaltic dikes crosscut the gabbros with irregular chilled boundaries, locally dissecting and embaying portions of the host rock (e.g., TA-02/Dy-1; see Fig. 2c of ref. 30). These basalts display a chemical composition indicative of limited fractionation in magma chambers and nearly flat PM-normalized incompatible trace element patterns, akin to present-day enriched MORBs[31] (Fig. 2). Being close to chemical equilibrium with the clinopyroxene from the most primitive gabbros, these basalts are considered poorly fractionated mantle melts that escaped crustal contamination and were injected into the cooling gabbroic crystal mush soon after its emplacement[30].

Radiogenic isotopes

The Tihama Asir gabbros exhibit higher initial (i.e., present-day values recalculated to their crystallization age; Supplementary Data S3) $^{87}Sr/^{86}Sr_{(i)}$ (0.7033–0.7037) and lower initial $^{143}Nd/^{144}Nd_{(i)}$ (0.51292–0.51296) ratios compared to those of Red Sea MORB[32–34] and the Cenozoic alkaline magmatism in the northern Arabian plate[19,20,35–40]. Nonetheless, their initial $^{206}Pb/^{204}Pb_{(i)}$ and $^{207}Pb/^{204}Pb_{(i)}$ ratios plot amongst the most depleted samples from the Red Sea MORB and the Cenozoic volcanism from northern Arabia (Fig. 3). The gabbros isotopically resemble the inferred compositions of the Afar plume[41–43] in terms of Nd and Sr isotopes, albeit they are less radiogenic in Pb. These compositions (Supplementary Data S3) suggest a source with relatively high time-integrated Rb/Sr and low Sm/Nd ratios compared to those of the northern Red Sea basalts, but with similarly low U–Th/Pb ratios. Interestingly, a basaltic dike (TA-02/Dy-1) cutting across the gabbros exhibits Sr–Nd–Pb isotopes nearly coincident with those of the inferred Afar plume (Fig. 3), supporting the idea that primary melts of the Tihama Asir formed from an asthenospheric source near the main impingement area of the Afar plume[30]. Upon closer examination, selected gabbroic samples gradually diverge from the crosscutting dike along trends of decreasing Sr–Nd and Pb isotope

https://doi.org/10.1038/s41467-025-61598-0

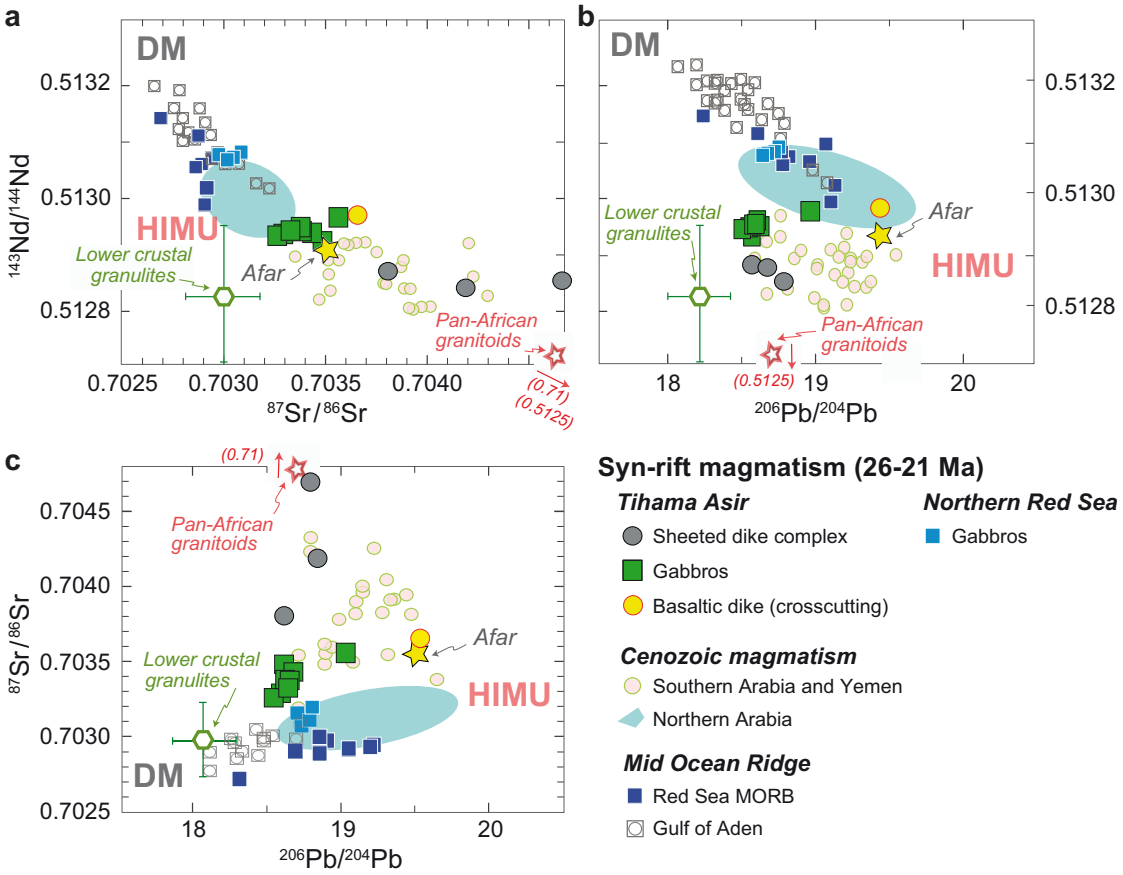

Fig. 3 | Initial Nd–Sr–Pb isotope compositions of the syn-rift magmatism in the Red Sea system compared to the Arabian Cenozoic volcanism and MORB. $^{143}Nd/^{144}Nd$, $^{87}Sr/^{86}Sr$ and $^{206}Pb/^{204}Pb$ ratios of Tihama Asir samples are recalculated to the average age of their formation (Supplementary Data S3). The yellow-filled circle indicates the composition of sample TA-02/Dy-1, taken from a basaltic dike that crosscuts the layered gabbros. For comparison, the average isotopic compositions of lower crustal granulite xenoliths[42], Pan-African granitoids[45], and the inferred compositions of the Afar Plume[43] are provided together with data for the northern Saudi Arabian lava fields (Harrat Rahat, Harrat Khaybar, Harrat Lunayyir, Harrat Kurama, Harrat Kishb, Harrat Tufil[19,20,37,39]); from southern Saudi Arabia and Yemen[34,37,42], and MORB data from the Red Sea axial trough and Gulf of Aden[32–34,90]. **a** $^{143}Nd/^{144}Nd$ versus $^{87}Sr/^{86}Sr$. **b** $^{143}Nd/^{144}Nd$ and **c** $^{87}Sr/^{86}Sr$ versus $^{206}Pb/^{204}Pb$. Error bars represent 1σ standard deviations.

ratios. These isotopic signatures suggest contamination by material with ancient depletions in Rb/Sr and U/Th/Pb, coupled with relatively low Sm/Nd ratios, compositions commonly attributed to lower continental crustal material, such as the ancient lower crustal granulite xenoliths locally sampled within the Cenozoic volcanism of the Arabian plate[25].

In contrast, samples from the sheeted dike complex have much higher initial $^{87}Sr/^{86}Sr_{(i)}$ (0.7038–0.7047) and lower initial $^{143}Nd/^{144}Nd_{(i)}$ (0.51284–0.51293) ratios compared to those of gabbros, yet they exhibit similar Pb isotope ratios. These samples cluster within the Nd–Sr and Pb isotopic space of the widespread volcanism in South Arabia and Yemen, well-known examples of Afar-type magma strongly contaminated by both upper and lower continental crust[41,42]. Given that these rocks display intrusive contacts with upper crustal lithologies and show selective enrichments in highly incompatible elements and LREE compared to the gabbros, we infer that their melts were generated within melt-rich zones of the gabbroic crystal mush and might have further assimilated Pan-African upper continental crust. Indeed, their Sr–Nd-Pb compositions fall between those of the Tihama Asir intrusives and the Pan-African granitoids (Fig. 3). Our hypothesis is corroborated by combined radiogenic Nd–Sr–Pb and $\delta^{18}O$ isotopes of flood volcanics from Yemen[42], which exhibit the same extent of isotopic variations observed in the Tihama Asir gabbros (Fig. 3). The less contaminated Yemenite basalts retain mantle-like $\delta^{18}O$ isotopes and Sr–Nd and Pb isotopic ratios indicative of an Afar-like upper mantle. In contrast, those retaining evidence of crustal contamination have high $\delta^{18}O$ isotopes[42] and diverge along two different trends, aligned towards enriched and depleted Pb compositions, indicating contamination by upper and lower Pan-African crust, respectively.

Assimilation-fractional crystallization model

We conducted assimilation-fractional crystallization (AFC) modeling following the approach outlined by ref. 44. Specifically tailored to simulate the chemical evolution of a magmatic system undergoing fractional crystallization alongside assimilation of wall rocks (Figs. 4 and 5). We utilized the average compositions of lower crustal granulite xenoliths[42] and Pan-African granitoids[45] as the assimilated components, and the crosscutting basaltic dike displaying Afar-like compositions as the initial melt (for further details, see Methods). The isotopic trends observed in the Tihama Asir gabbros are faithfully reproduced across all different Nd–Sr–Pb isotopic spaces at low degrees of assimilation of lower crustal granulites, considering mass assimilated/mass crystallized ratios ranging from 0.7 to 0.9 (Fig. 4), and utilizing the same geochemical parameters used to replicate the trace element enrichments[30].

Conversely, the high Sr and low Nd isotopes observed in the sheeted dikes necessitate additional assimilation of Pan-African

https://doi.org/10.1038/s41467-025-61598-0

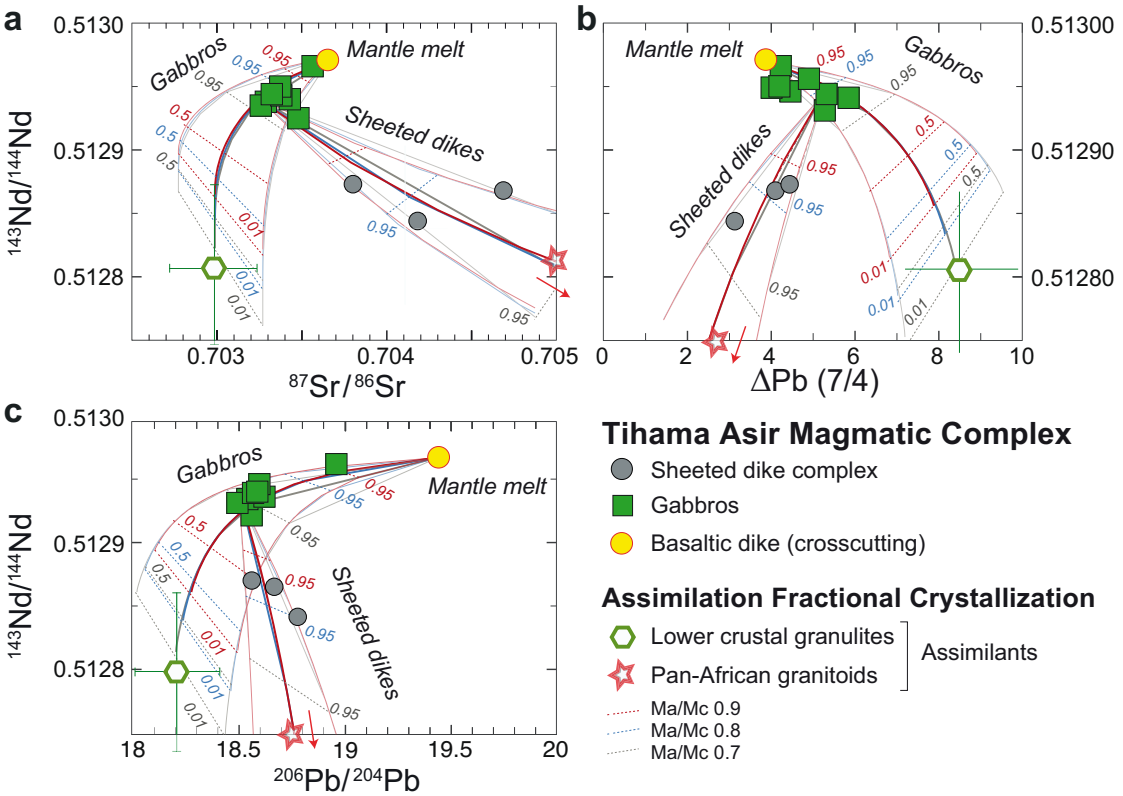

Fig. 4 | Results of the assimilation-fractional crystallization models in the Nd-Sr-Pb isotope space compared to the Tihama Asir gabbros and associated dike swarm. $^{143}Nd/^{144}Nd$, $^{87}Sr/^{86}Sr$ and $^{206}Pb/^{204}Pb$ ratios of Tihama Asir samples are recalculated to the average age of their formation (Supplementary Data S3). The yellow-filled circle indicates the composition of sample TA-02/Dy-1, taken from a basaltic dike that crosscuts the layered gabbros. The AFC models are calculated at assimilated mass/crystallized mass (Ma/Mc) ratios of 0.9, 0.8, and 0.7, depicted by red, blue, and green lines, respectively (Supplementary Data S4). Bold lines represent AFC trends using the average values of lower crustal granulites and Pan-African granitoids, while thin lines indicate AFC trends calculated for extreme (±1σ) compositions. Remaining melt mass is traced on each trend by dashed lines, indicated by italic numbers. **a** $^{143}Nd/^{144}Nd$ versus $^{87}Sr/^{86}Sr$. **b** $^{143}Nd/^{144}Nd$ versus ΔPb (7/4). **c** $^{143}Nd/^{144}Nd$ versus $^{206}Pb/^{204}Pb$. Error bars are shown in 1σ when available.

granitoids, commencing from the hybrid melts that formed the gabbros. Notably, our model adeptly reproduces the distinct trends of the gabbros and dike swarms concerning Nd and Sr versus ΔPb (7/4) (Fig. 4b). The low $^{206}Pb/^{204}Pb$ ratios and comparatively high $^{207}Pb/^{204}Pb$ ratios of lower crustal granulites in the Arabian plate[42] result in a gradual increase in ΔPb (7/4) as $^{143}Nd/^{144}Nd$ ratios decrease. Conversely, the upper crustal Pan-African granitoids have $^{206}Pb/^{204}Pb$ and $^{207}Pb/^{204}Pb$ lying on the NHRL[45], thus producing a local decrease in ΔPb (7/4).

Discussion

The evolution of the Red Sea rift has been debated for over 50 years, with no definitive evidence confirming the nature of the underlying crust[14,46]. Even in recent publications, strong uncertainty remains regarding the extent of oceanic crust within the basin. Some researchers support a fully oceanic regime extending along the entire Red Sea basin since 14–10 Ma[46–48], while others propose that attenuated continental crust persisted until 6–5 Ma, when seafloor spreading initiated in the southern and central Red Sea[49–51]. Both hypotheses are based on similar datasets, including magnetic, gravity, bathymetric, and seismic data, yet no borehole samples exist to conclusively determine the nature of the crust beneath the main trough. Furthermore, gravity and magnetic signatures are ambiguous and can be attributed to either oceanic or continental sources. The thick, high-velocity evaporite sequence also limits the resolution of multichannel seismic reflection profiles, obscuring the basement's tectonic architecture and hindering efforts to resolve its origin.

Crustal contamination and magmatic underplating

Earlier studies proposed that seafloor spreading in the southern Red Sea began with the emplacement of the Tihama Asir and Al Lith magmatic complexes (26–21 Ma), where gabbros and dikes, with a strong geochemical affinity to melts generated by depleted mantle, could indicate emplacement of oceanic crust beneath much of the Red Sea's coastal plains, shelf regions and its central axis[26,52,53]. Our results show that syn-rift gabbros formed in relatively shallow magma chambers[12,30], fueled by asthenospheric melts that incorporated ancient lower continental crust material, but show no evidence of interactions with continental mantle material. The minimal contamination from upper crustal material suggests these melts ascended rapidly through the continental crust with limited interaction. Volatile incorporation (CO_2, H_2O) may have facilitated melt migration through the extending continental crust[12]. In contrast, the sheeted dikes display higher contamination from continental material, including the upper crust. Trapping of silica undersaturated basaltic melts in the upper crust and crustal anatexis has led to the formation of peralkaline granitic magmas[11,54]. The geochemical composition of the Tihama Asir primitive gabbros and cross-cutting dykes indicate a rapid replacement of the continental lithospheric mantle with upwelling asthenosphere, where depleted mantle melts initially pooled at depth as sills/batholiths within the lower continental crust before rising to shallower levels through dikes during the early phases of Red Sea rifting. This process is also supported by gravity models explaining Bouguer anomaly patterns[51].

Geophysical data, including density, magnetic and seismic velocity anomalies, provide strong constraints on the presence and extent

https://doi.org/10.1038/s41467-025-61598-0

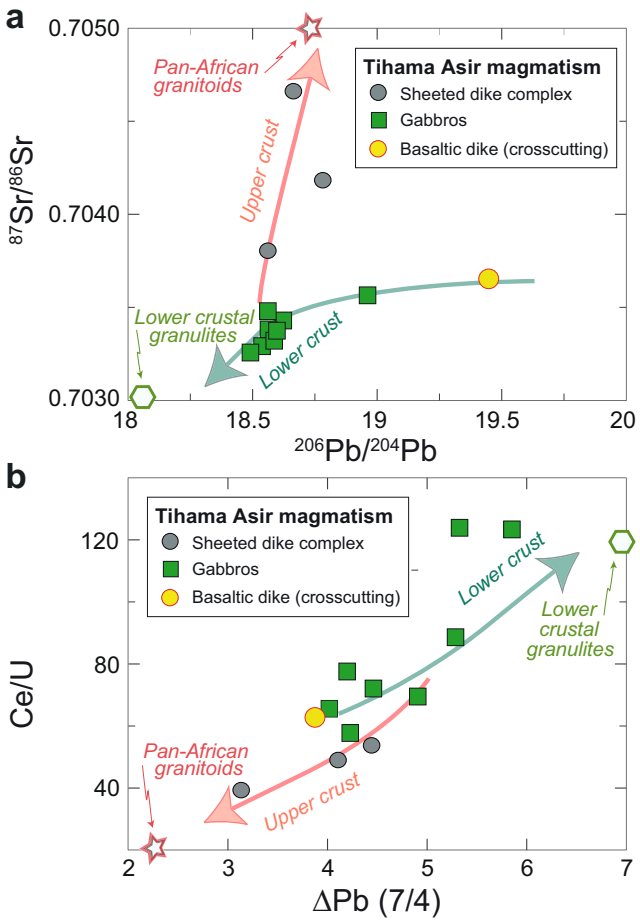

Fig. 5 | Variation in Sr–Pb isotopes and Ce/U ratios in the Tihama Asir gabbros and the associated sheeted dike complex. a $^{87}Sr/^{86}Sr$ vs $^{206}Pb/^{204}Pb$ ratios, recalculated to the average formation age (Supplementary Data S3). **b** Ce/U vs ΔPb(7/4) ratios. Trends indicating assimilation of Pan-African granitoids[45] (light red arrow) and lower crustal granulites[42] (light green arrow) are also shown (Supplementary Data S4). Symbols are consistent with those in Fig. 4.

of magma underplating within the southern Red Sea rift. A positive Bouguer gravity anomaly of ~30 mGal along the Arabian coast (Supplementary Fig. S2) suggests the presence of a high-density body at the base of the crust[51]. This finding is in line with observations of high seismic velocities in the lower crust[55,56], which is underlain by a low-velocity upper mantle[57], as observed beneath the southwestern Arabian coastal plain. In addition, thermal uplift caused by the rising asthenosphere and underplating beneath the Arabian margin may explain the observed asymmetry of early syn-rift magmatism and rift flanking escarpments on the conjugate margins[58,59].

In the southern Red Sea, high-frequency, high-amplitude reduced-to-the-pole magnetic anomalies (RTP) associated with seafloor spreading are distinctly discernible up to Chron 3A near the axial trough between 16°N and 19°N, suggesting that seafloor spreading commenced ~5 Ma[58]. Long-wavelength low-amplitude RTP anomalies running over the Arabian shelf, subparallel to the coastline from the Farasan Islands to the coastal plain (Fig. 6a), have been previously interpreted as seafloor spreading magnetic stripes, leading to the hypothesis that the Red Sea formed through two stages of seafloor spreading: the first phase during the Late Oligocene-Early Miocene (~28–23 Ma) and the second phase post-Miocene (~5–0 Ma)[26,52,53]. Our results indicate that this interpretation, besides not aligning with the age of early syn-rift magmatic rocks (26–21 Ma) and with inferred crustal thickness (35-40 km) beneath the coastal plain[56] would imply unrealistic full spreading rates of 44 mm/yr during the first seafloor spreading episode[53], which contradict the estimated initial rate of extension across the Red Sea rift (Late Oligocene-Early Miocene), approximately half of present-day values (<10 mm/yr)[60]. Seismic surveys for hydrocarbon exploration beneath the southern Saudi Arabia coastal plain (15°–21°N) reveal that Miocene and younger sediments lie unconformably over Late Oligocene-Miocene volcanoclastic deposits of the Jizan Group formation, which are intruded by dense swarms of subvertical mafic dikes trending from N to NW[61] (Fig. 6b). Hence, an alternative explanation for the long-wavelength, low-amplitude RTP anomalies, supported by the high remanent magnetization (average NRM > 4.5 A/m) of the studied samples from the Tihama Asir magmatic complex, with a Koenigsberger ratio almost consistently above one (Supplementary Fig. S3), could involve the continuous and widespread intrusion of mafic melts into the upper continental crust, progressively migrating over 20–15 million years toward the distal part of the evolving rift. When geomagnetic reversals occur more frequently (61 reversals within the time interval between chrons 5 and 6C, ~24–10 Ma[62]) than the cooling and intrusion times of magmatic rocks, the resulting magnetic anomalies can combine to produce low-frequency, low-amplitude magnetic signatures.

Our findings are crucial because, until now, most constraints on the location and depth of magma intrusions during the initial stages of rifting have been derived from crustal-scale seismic imaging of relatively young (e.g., Ethiopian) and poorly evolved (e.g., Baikal) rifts. Seismic evidence from the Baikal rift indicates mafic intrusions in the lower crust without corresponding intrusions in the upper crust during the early stages of the rift[63], similar to what has been proposed for the northern Red Sea[13,14]. Wide-angle seismic refraction data collected in the more evolved Ethiopian rift reveal high seismic velocities over a large lower crustal region beneath the rift, suggesting abundant intrusions. However, the mid-upper crust exhibits a narrow zone of elevated seismic velocities confined to the present-day rift axis[64]. Satellite geodesy reveals rift-scale deformation in the Afar rift caused by magmatic intrusions in the deep crust, with magmatic additions occurring through a network of sills[65]. These geophysical observations provide important constraints on the processes responsible for the formation of thick igneous crust beneath magma-rich rifted margins and are consistent with our petrological evidence from the southern Red Sea.

Magma-assisted extension during rifting

Although several questions remain, our work allows to outline the evolution of the southern Red Sea rift and the transition from continental rifting to oceanic seafloor spreading, driven by interactions between thermal, structural and magmatic processes (Fig. 7). A possible explanation for the different lithospheric extension responses between the northern and southern Red Sea is the thermal erosion and weakening of the continental lithosphere as a result of the Afar plume head which impacted the area around 34 Ma. Although the most intense volcanic activity associated with the plume occurred in Ethiopia and southern Yemen, widespread contemporaneous volcanism has also been recorded as far north as 20°N, in the Red Sea Hills of Eritrea and Sudan[66,67]. At the end of the Oligocene (~29 Ma)[15], the plume-related thermal weakening of the continental lithosphere and dynamic uplift in the Red Sea region, combined with far-field tectonic forces associated with the initiation of the Zagros subduction[5] led to the stretching and thinning of the lithosphere. This process resulted in the formation of extensional shear zones along the margins and the passive upwelling of the asthenosphere beneath the rift axis.

We show here that the rise of asthenosphere enabled the rapid replacement of the continental lithospheric mantle, as indicated by the geochemical and isotopic compositions of the Tihama Asir primitive gabbros and dykes cross-cutting the gabbro bodies, which show no

https://doi.org/10.1038/s41467-025-61598-0

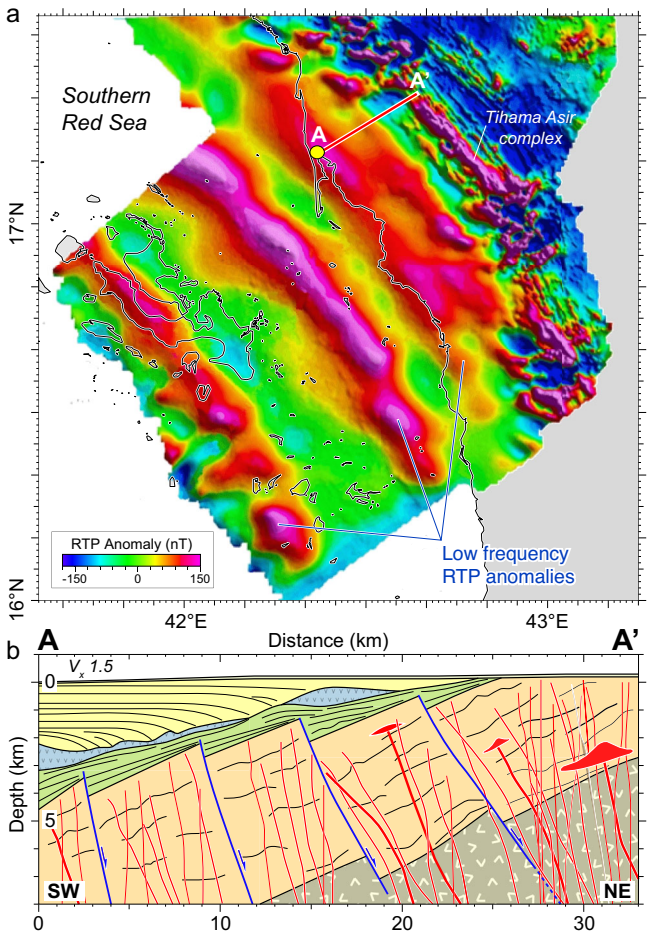

Fig. 6 | Magnetic anomalies of the Tihama Asir region and adjacent Red Sea. **a** Reduced-to-the-pole (RTP) aeromagnetic data "(from ref. 25)" displaying the long-wavelength, low-amplitude magnetic anomalies that characterize the Tihama Asir coastal plain and the Red Sea eastern margin. The thick red solid line indicates the location of the cross-section A-A' shown in (**b**). The yellow circle shows the location of the deep Mansiyah-1 oil-well[61]. Mercator projection at 17°N, datum WGS84. Spatial analysis and mapping were carried out using the PLOTMAP package[87]. **b** Simplified geologic cross-section running SW-NE from the coast to the Tihama Asir magmatic complex, with a vertical exaggeration of 1.5. Geological data from ref. 61. Light olive pattern represents the Precambrian basement; light orange filled area corresponds to the Oligocene Jizan Group; green solid filled area depicts Miocene pre-rift sediments; cyan patterns indicate halite deposits; yellow and light yellow filled areas show Mio-Pliocene and Quaternary sediments, respectively. Faults are represented by blue solid lines, while dikes and sills are shown by red solid lines and red filled areas, respectively.

evidence of interaction with continental mantle but only assimilation of lower crust material. The ascent of asthenosphere resulted in decompression partial melting, producing tholeiitic melts that underplated the lower continental crust and fed the gabbroic intrusions and basaltic dikes of the Tihama Asir and Al Lith magmatic complexes, as well as the dike swarms extending along the entire Red Sea coast of Arabia[5]. Plume-related thermal anomalies and underplating may have initially weakened the lower crust, allowing decoupling between the lower crust and the lithospheric mantle along the axial zone beneath the thinning upper continental lithosphere (Fig. 7). The combination of thermal softening and ductile flow of the lower crust possibly led to depth-dependent, less localized and more distributed deformation, protracting crustal extension and favoring the development of a wide rifted margin[51,68,69] (i.e., Type II of ref. 68.) At low extension rates, when migrating melt does not repeatedly intrude the same axial zone, dike intrusions may have weakened less the upper crust[70] increasing crustal strength compositionally[14]. This process can accommodate extension in the crust, maintain its thickness, and delay crustal rupturing. The interaction between mantle plume upwelling and extensive lower crustal magmatic intrusions within the slowly diverging Nubia-Arabia continental lithosphere probably contributed to rift initiation, accommodating plate separation by re-thickening the thinned lower crust and compensating for extension through widespread dike intrusions in the upper crust. Continued extension processes and magmatic additions further widened the Red Sea basin and caused rift axis focusing, with localization of deformation controlled by strength contrast between weakened and non-weakened regions[71,72]. Seafloor spreading commenced approximately 15-20 Ma later than the start of rifting, in the axial trough of the southern Red Sea, leading to the formation of new oceanic crust from MORB magmas (Supplementary Fig. S4).

Protracted rifting, resulting from the breakup of the mantle lithosphere during the initial stages of rifting while the crust undergoes extended stretching, has also been suggested in other magma-rich rift settings such as the Afar Depression[73] and the North Atlantic[74]. For instance, in the Afar Depression, early magmatic intrusions helped maintain crustal thickness during the initial stages of rifting, while final rupture and the onset of seafloor spreading were triggered by late-stage thinning of an already intruded and mechanically weakened lithosphere[73]. This process closely parallels the evolution we infer for the southern Red Sea, where long-lived magmatic activity played a central role in facilitating rift development and prolonging the phase of continental extension prior to final breakup (Supplementary Fig. S4). Similarly, in the North Atlantic, seismic imaging reveals that large volumes of melt were intruded as sills into the lower crust within a narrow continent–ocean transition zone, highlighting the dominant role of intrusive magmatism in shaping rift architecture[74]. These observations support the interpretation that elevated mantle temperatures were the primary driver of melt production[74], consistent with our model, in which plume-related thermal anomalies, magmatic underplating, and magmatic additions facilitated magma-assisted extension.

Our results indicate that mafic underplating and the assimilation of pre-existing continental lithosphere are important processes for the transformation of continental crust into proto-oceanic crust. Magmatic intrusions in the lower crust delay the localization of lithospheric extension and the final drifting stage by several million years, until continental breakup results in the establishment of a steady-state spreading center. At this stage, high-frequency magnetic anomalies typical of an oceanic crust form parallel to the ridge axis, associated with a negative seismic velocity anomaly localized along the active spreading center.

Methods

$^{40}Ar/^{39}Ar$ dating

Age determinations were performed at the Laboratoire des Sciences du Climat et de l'Environnement facility (CNRS-CEA, Gif-sur-Yvette), France.

Sample preparation

$^{40}Ar/^{39}Ar$ measurements were performed on the microcrystalline groundmass of the sample, considered representative of the phase that crystallized during lava solidification. Samples were crushed, sieved (250–125 mm size), and washed in 1 N acetic acid at 60 °C for 40 minutes to remove secondary mineral phases. Phenocrysts and xenocrysts, carrying an excess of ^{40}Ar, were removed using heavy liquids (Diiodomethane) and magnetic separations. Absence of alteration phases was verified using a binocular microscope.

Procedure

Splits of 120–130 mg were wrapped in 99.5% copper foil, loaded in aluminum disks, and irradiated in the CLICIT facility at Oregon State

https://doi.org/10.1038/s41467-025-61598-0

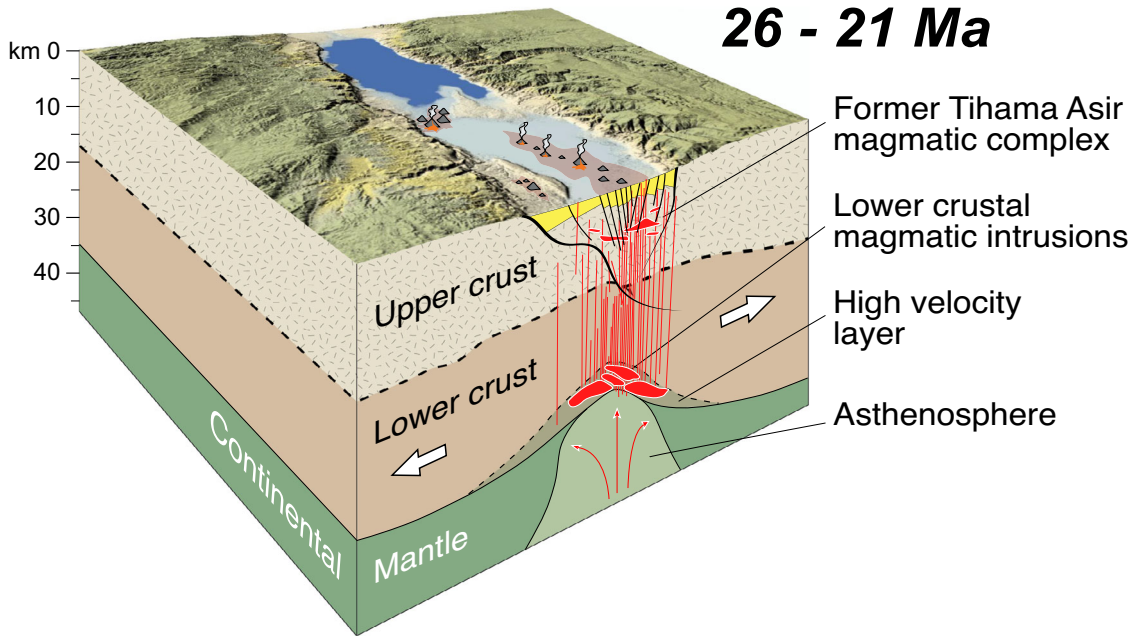

Fig. 7 | Initial stages of the rifting process in the Southern Red Sea. Weakening processes within the lower crust play a crucial role in controlling rift evolution. During the early stages of the Red Sea rift, thermal weakening of the lower crust, driven by the Afar plume thermal anomaly, may have facilitated decoupling between the lower crust and the continental mantle. This possibly resulted in depth-dependent deformation that was less localized, more distributed, and led to the production of abundant asthenospheric melt, which underplated and intruded the thinning continental lithosphere along the axial zone. The interaction between mantle plume upwelling and extensive lower crustal magmatic intrusions within the slowly diverging Nubia-Arabia continental lithosphere contributed to the initiation and evolution of the Red Sea rift, accommodating plate separation by re-thickening a thinned lower crust and compensating for crustal extension through magmatic additions. Spatial analysis and mapping of the proposed early-rift elevation data were conducted using the PLOTMAP package[87].

University's TRIGA reactor for 10 h. After irradiation, samples were degassed at 550-650 °C to remove atmospheric argon. Neutron fluence (J) was monitored using FCs crystals, with J values calculated from 6 single crystal laser fusion analyses, reported in Supplementary Data S1. Age calculations used the decay constants from ref. 75 and an atmospheric $^{40}Ar/^{36}Ar$ ratio of 298.56 from ref. 76. Precision of mass discrimination correction was monitored by daily air argon measurements, achieving about 0.1–0.15% (1σ standard deviation).

Pure groundmass aliquots were incrementally heated in 10 steps between 650 °C and 1200 °C using a metal resistance furnace. Isotopic measurements were performed using a high-sensitivity GV5400 instrument in ion counting mode. An analytical run consisted of 20 peak scans of each argon isotope with integration times 2 s (^{40}Ar, ^{39}Ar), 10 s (^{37}Ar, ^{38}Ar, baseline) and 20 s (^{36}Ar). This was preceded by a peak centering routine on the five Ar isotopes upon sample admission into the mass spectrometer. Raw argon isotope abundances were regressed back to inlet time using NG software (v. 2.90). System blanks measured prior to step-heating ranged from 6.8×10^{-16} to 1.2×10^{-15} moles of ^{40}Ar and $2.5{\cdot}10^{-18}$ to 6.2×10^{-18} moles of ^{36}Ar, which were substantially lower than sample signals.

Results

Plateau ages, isochron regressions, probability of fit estimates and errors were calculated using ArArCalc[77] following the criteria defined in ref. 78. Results of the step heating experiment are detailed in the Supplementary Data S1. The plateau age for sample TA-06/Dy-1, calculated from 66.4% of gas released, excluded the first three and last steps due to anomalously young apparent ages likely caused by $^{40}Ar^*$ loss from subtle alteration. The preferred age for this sample is the plateau age of 26.03 ± 0.54 Ma (2σ uncertainty).

Re-evaluation of Ar–Ar literature dates using updated standards

$^{40}Ar/^{39}Ar$ ages from ref. 28. were originally calibrated against an age of 17.25 ± 0.20 Ma for the Bern 4B biotite standard, which corresponds to an age of 126.6 ± 4.2 Ma for LP-6[79]. Initially, Bern 4B's age was recalibrated using the ArAR software[80], considering an updated age of 127.5 Ma for LP-6, which equates to an age of 28.10 ± 0.04 Ma for FCTs. This recalibration increased the age of Bern 4B to 17.38 ± 0.20 Ma. This age was further recalculated using the FCTs age applied in this study (28.201 ± 0.023 Ma[81]). Based on this calculation, the age of Bern 4B is adjusted to 17.44 ± 0.20 Ma. This updated age was used to recalculate the ages reported by ref. 28. using the ArAR software. For consistency, we also applied the constant values from ref. 75. in the calculation (Supplementary Data S1).

Bulk rock major, trace elements, and Sr, Nd, and Pb isotope compositions

The bulk rock major and trace element compositions of the Tihama Asir gabbros and sheeted dikes are sourced from ref. 30. and were analyzed using XRF and ICP-mass spectrometry at Activation Laboratories Ltd., Ancaster, Ontario (Supplementary Data S2), following the analytical techniques detailed on the company's website (www.actlabs.com).

Bulk rock Sr, Nd, and Pb isotope analyses were conducted at the Dipartimento di Scienze della Terra, University of Florence. Sample powders (approximately 250 mg each) were taken from the same aliquots used for major and trace element determinations. The samples were leached with 1 M HCl in an ultrasonic bath and rinsed several times with MilliQ water to minimize potential contributions from secondary phases that could have altered the magmatic signature. The samples were dissolved through sequential HF–HNO_3–HCl dissolution, and the Sr, Nd, and Pb fractions were purified through standard liquid chromatographic techniques.

Isotopic ratios were determined using thermal ionization mass spectrometry (Thermo-Fisher Scientific Triton Plus). Mass fractionation of Sr and Nd isotopes was exponentially corrected with $^{86}Sr/^{88}Sr = 0.1194$ and $^{146}Nd/^{144}Nd = 0.7219$, respectively. Interferences of ^{87}Rb and ^{144}Sm on ^{87}Sr and ^{144}Nd, respectively, were monitored by measuring ^{85}Rb and ^{147}Sm. Due to their extremely low abundances

(when present) these masses were measured on 10^{13} Ohm amplifiers; such interferences resulted negligible for all the samples. All other masses were measured on 10^{11} Ohm amplifiers. The within-run $^{87}Sr/^{86}Sr$ average value for NBS 987 reference material was 0.710255 ± 7 (2σ, n = 4), and the $^{143}Nd/^{144}Nd$ average value for the internal standard NdFi was 0.511465 ± 3 (2σ, n = 3). Accuracy and precision were further checked by measuring the isotope ratios of international rock standards BHVO-1 ($^{87}Sr/^{86}Sr$ = 0.703484 ± 6; $^{143}Nd/^{144}Nd$ = 0.512986 ± 9) and BCR-2 ($^{87}Sr/^{86}Sr$ = 0.705018 ± 7; $^{143}Nd/^{144}Nd$ = 0.512620 ± 5).

Lead isotopic composition was measured by collecting the smaller ^{204}Pb beam on 10^{13} Ohm amplifier and the other masses (^{206}Pb, ^{207}Pb, and ^{208}Pb) on 10^{11} Ohm amplifiers. Instrumental mass bias was corrected using replicate analyses of NIST SRM 981 standard, yielding an average fractionation factor of 0.135% (±0.010%) per mass unit relative to the reference values, which was applied to all Pb isotopic ratios. The accuracy of the Pb isotope measurements was tested through replicate analyses of international reference material BHVO-1 ($^{206}Pb/^{204}Pb$ = 18.705 ± 4, $^{207}Pb/^{204}Pb$ = 15.577 ± 5, $^{208}Pb/^{204}Pb$ = 38.375 ± 15). All the measured isotope ratios of the reference materials are reported in Supplementary Data S3 and are identical within error to previously published values[82,83].

All the isotope ratios were recalculated to their initial values, assumed to correspond to the time of the rock formation. The formation ages of the studied samples were estimated based on the available Ar–Ar ages of the associated lithological units (this work and recalibrated ages of ref. 28. (Supplementary Data S1). For the age correction, we specifically re-measured the elemental Rb/Sr, Sm/Nd, U/Pb, and Th/Pb ratios on the leached samples using ICP-MS (7800 Agilent) at the University of Florence. A small aliquot of the same sample solution used for isotopic measurements was collected (after complete dissolution and before chemical separation), evaporated, and diluted in 2% HNO_3 for ICP-MS analyses. Replicate analyses of international reference materials BHVO-1 and AGV-1 yielded Rb/Sr, U/Pb, Th/Pb, and Sm/Nd ratios consistent with reference values of ref. 84. and with reproducibility <4% (2σ). The internal errors (2σ) of the age-corrected Sr, Nd, and Pb isotope ratios for all samples were fully propagated to account for uncertainties in age, isotopic ratios, and elemental contents. Total procedure blanks for Sr, Nd, and Pb were 60 pg, 12 pg, and 43 pg, respectively. The data and associated uncertainties are reported in Supplementary Data S3.

Assimilation-fractional crystallization model

The enrichments in highly incompatible elements (e.g., Rb, Ba, Th, U, Zr, Hf) and the positive LREE/HREE fractionation observed in the melts in equilibrium with the Tihama Asir clinopyroxenes can be effectively reproduced by a process involving the assimilation of lower and upper continental crust, combined with fractional crystallization of a gabbroic assemblage (i.e., olivine, plagioclase, and clinopyroxene)[30]. A similar geochemical model is applied here to assess whether the assimilation of lower and upper continental crust can explain the isotopic compositions of the Tihama Asir gabbros and the associated sheeted dike.

The trace element (Sm, Nd, Rb, Sr, Th, U, and Pb) and initial Nd–Sr–Pb isotopic compositions of the melts generated during the two scenarios above (assimilation of lower and/or upper crust) were calculated using an assimilation-fractional crystallization (AFC) process, following the equations of ref. 44. For the assimilation of the lower crust, we used the basalts (TA-02/Dy-1) crosscutting the Tihama Asir gabbros at a high angle as the starting melt composition. These basalts, unmodified by any crustal contamination process, exhibit an EMORB-like trace element pattern and an isotopic composition similar to that of the inferred Afar plume[43]. Conversely, the starting melt composition for the assimilation of upper crust has a Nd–Sr–Pb isotopic composition coinciding with the average isotopic composition of the Tihama Asir gabbros and is similar to melts extracted from the gabbros after 5–10% degrees of lower crustal contamination. The composition of the melt modified by the AFC process was calculated at 1% increments, representing the remaining melt mass (scaled from 100% to 0), corresponding to 'F' in the equation from ref. 44. Each of the two AFC scenarios was calculated using the mean and extreme (±1σ) compositions of the lower and upper crust assimilants[42,45]. The AFC scenarios were modeled with different Ma/Mc ratios of 0.9, 0.8, and 0.7, shown in Fig. 4 in red, blue, and gray, respectively. Parameters and results are provided in Supplementary Data S4.

Magnetic properties

Magnetic properties, including natural remanent magnetization (NRM) and volume-specific magnetic susceptibility (K), were measured on 14 rock samples at the paleomagnetic lab of ISMAR-CNR in Bologna, Italy. Four samples (marked AR) of basaltic dikes were hand-oriented in the field using a magnetic compass. In the laboratory, between 1 and 5 standard paleomagnetic cylinders (2.54 × 2.2 cm) were drilled from each rock sample, resulting in a total of 31 specimens. The NRM was measured with a PSM spinner magnetometer, while magnetic susceptibility (K) was determined using a Bartington MS2B meter. The Koenigsberger ratio (Q) was calculated as the ratio of remanent magnetization (NRM) to the induced magnetization produced by Earth's field (26.506 A/m). Results are presented in Supplementary Fig. S3 and Supplementary Data S5.

Data availability

All the data generated in this study are provided in the Supplementary Data files (from S1 to S5) and have also been deposited in Figshare https://doi.org/10.6084/m9.figshare.29410169.

Code availability

The Assimilation-fractional crystallization (AFC) model code (alphaMELTS), which can be used to re-produce the data presented here (Supplementary Data S4), is available on *GitHub* https://github.com/magmasource/alphaMELTS.

References

1. Wilson, J. T. Did the Atlantic Close and then Re-Open?. *Nature* **211**, 676–681 (1966).
2. Gurnis, M. Large-scale mantle convection and the aggregation and dispersal of supercontinents. *Nature* **332**, 695–699 (1988).
3. Hofmann, C. et al. Timing of the Ethiopian flood basalt event and implications for plume birth and global change. *Nature* **389**, 838–841 (1997).
4. Ebinger, C. J. & Sleep, N. H. Cenozoic magmatism throughout East Africa resulting from impact of a single plume. *Nature* **395**, 788–791 (1998).
5. Bosworth, W., Huchon, P. & McClay, K. The Red Sea and Gulf of Aden basins. *J. Afr. Earth Sci.* **43**, 334–378 (2005).
6. Roeser, H. A. A detailed magnetic survey of the southern Red Sea. *Geol. Jahr.* **D13**, 131–153 (1975).
7. Bonatti, E. Punctiform initiation of seafloor spreading in the Red Sea during transition from continental to an oceanic rift. *Nature* **316**, 33–37 (1985).
8. Cochran, J. R. Northern Red Sea: Nucleation of an oceanic spreading center within a continental rift. *Geochem. Geophys. Geosyst.* **6**, Q03006 (2005).
9. Viltres, R. et al. Present-day motion of the Arabian plate. *Tectonics* **41**, e2021TC007013 (2022).
10. Baker, J. A., Thirlwall, M. F. & Menzies, M. A. Sr-Nd-Pb isotopic and trace element evidence for crustal contamination of plume-derived flood basalts: Oligocene flood volcanism in western Yemen. *Geochim Cosmochim. Acta* **60**, 2559–2581 (1996).
11. Manetti, P. et al. Magmatism of the eastern Red Sea margin in the northern part of Yemen from Oligocene to present. *Tectonophysics* **198**, 181–202 (1991).

12. Coleman, R. G. & McGuire, A. V. Magma systems related to the Red Sea opening. *Tectonophysics* **150**, 77–100 (1988).
13. Ligi, M. et al. Birth of an Ocean in the Red Sea: oceanic-type Basaltic Melt Intrusions Precede Continental Rupture. *Gondwana Res.* **54**, 150–160 (2018).
14. Ligi, M., Bonatti, E., Bosworth, W. & Ronca, S. Oceanization starts at depth during continental rupturing in the northern Red Sea. in: *Geological setting, Palaeoenvironment and Archaeology of the Red Sea* (eds Rasul, N. M. A. & Stewart, I. C. F.) pp 131–157 (Springer Earth Sciences Series, Springer-Verlag Berlin, 2019).
15. Bohannon, R. G. Style of extensional tectonism during rifting, Red Sea and Gulf of Aden. *J. Afr. Earth Sci.* **8**, 589–602 (1989).
16. Pallister, J. S. Magmatic history of Red Sea rifting: perspective from the central Saudi Arabian coastal plain. *Geol. Sot. Am. Bull.* **98**, 400–417 (1987).
17. Camp, V. E., Roobol, M. J. & Hooper, H. P. The Arabian continental alkali basalt province: part II. Evolution of Harrats Khaybar, Ithnayn, and Kura, Kingdom of Saudi Arabia. *Geol. Soc. Am. Bull.* **103**, 363–391 (1991).
18. Camp, V. E. & Roobol, M. J. Upwelling asthenosphere beneath western Arabia and its regional implications. *J. Geophys. Res.* **97**, 15255–15271 (1992).
19. Sanfilippo, A. et al. Hidden but Ubiquitous: the Pre-Rift Continental Mantle in the Red Sea Region. *Front. Earth Sci.* **9**, 699460 (2021).
20. Sanfilippo, A. et al. The Nubian-Arabian shield mantle and Cenozoic magmatism of western Arabia. in: *Rifting and Sediments in the Red Sea and Arabian Gulf Regions* (eds Rasul N. M. A. & Stewart I. C. F.) pp 37–60 (CRC Press, Taylor & Francis Group, Abingdon, Oxon, 2024).
21. Nielsen, T. K. & Hopper, J. R. From rift to drift: mantle melting during continental breakup. *Geochem. Geophys. Geosyst.* **5**, Q07003 (2004).
22. Armitage, J. J., Collier, J. S. & Minshull, T. A. The importance of rift history for volcanic margin formation. *Nature* **465**, 913–917 (2010).
23. Thybo, H. & Artemieva, I. M. Moho and magmatic underplating in continental lithosphere. *Tectonophysics* **609**, 605–619 (2013).
24. Lu, G. & Huismans, R. S. Melt volume at Atlantic volcanic rifted margins controlled by depth-dependent extension and mantle temperature. *Nat. Commun.* **12**, 3894 (2021).
25. Stern, R. J. & Johnson, P. Continental lithosphere of the Arabian Plate: A geologic, petrologic, and geophysical synthesis. *Earth Sci. Rev.* **101**, 29–67 (2010).
26. Stern, R. J. & Johnson, P. Constraining the opening of the Red Sea: evidence from the Neoproterozoic margins and Cenozoic magmatism for a volcanic rifted margin. in: *Geological Setting, Palaeoenvironment and Archaeology of the Red Sea* (eds Rasul N. M. A. & Stewart, I. C. F.) pp 53–79 (Springer Earth System Science Series, Springer Nature, Cham, 2019).
27. McGuire, A. V. & Coleman, R. G. The Jabal Tirf layered gabbro and associated rocks of the Tihama Asir complex. SW Saudi Arabia. *J. Geol.* **94**, 651–665 (1986).
28. Sebai, A. et al. $^{40}Ar/^{39}Ar$ dating of alkaline and tholeiitic magmatism of Saudi Arabia related to the early Red Sea Rifting. *Earth Planet. Sci. Lett.* **104**, 473–487 (1991).
29. Bosworth, W. & Stockli, D. F. Early magmatism in the greater Red Sea rift: timing and significance. *Can. J. Earth Sci.* **53**, 1158–1176 (2016).
30. Basch, V. et al. Crustal contamination and hybridization of an embryonic oceanic crust during the Red Sea rifting (Tihama Asir igneous complex, Saudi Arabia). *J. Petrol.* **63**, egac005 (2022).
31. Gale, A., Escrig, S., Gier, E. J., Langmuir, C. H. & Goldstein, S. L. Enriched basalts at segment centers: the Lucky Strike (37°17′N) and Menez Gwen (37°50′N) segments of the Mid-Atlantic Ridge. *Geochem. Geophys. Geosyst.* **12**, Q06016 (2011).
32. Schilling, J.-G., Kingsley, R. H., Hanan, B. B. & McCully, B. L. Nd-Sr-Pb isotopic variations along the Gulf of Aden—evidence for Afar mantle plume continental lithosphere interaction. *J. Geophys. Res.* **97**, 10927–10966 (1992).
33. Volker, F., McCulloch, M. T. & Altherr, R. Submarine basalts from the Red Sea: new Pb, Sr, and Nd isotopic data. *Geophys. Res. Lett.* **20**, 927–930 (1993).
34. Volker, F., Altherr, R., Jochum, K. P. & McCulloch, M. T. Quaternary volcanic activity of the southern Red Sea: new data and assessment of models on magma sources and Afar plume-lithosphere interaction. *Tectonophysics* **278**, 15–29 (1997).
35. Altherr, R., Henjes-Kunst, F. & Baumann, A. Asthenosphere versus lithosphere as possible sources for basaltic magmas erupted during formation of the Red Sea: constraints from Sr, Pb and Nd isotopes. *Earth Planet. Sci. Lett.* **96**, 269–286 (1990).
36. Stein, M. & Hofmann, A. W. Fossil plume head beneath the Arabian lithosphere?. *Earth Planet. Sci. Lett.* **114**, 193–209 (1992).
37. Bertrand, H., Chazot, G., Blichert-Toft, J. & Thoral, S. Implications of widespread high-m volcanism on the Arabian Plate for Afar mantle plume and lithosphere composition. *Chem. Geol.* **198**, 47–61 (2003).
38. Shaw, J. E., Baker, J. A., Menzies, M. A., Thirlwall, M. F. & Ibrahim, K. M. Petrogenesis of the largest intraplate volcanic field on the Arabian Plate (Jordan): a mixed lithosphere–asthenosphere source activated by lithospheric extension. *J. Petrol.* **44**, 1657–1679 (2003).
39. Moufti, M. R., Moghazi, A. M. & Ali, K. A. Geochemistry and Sr–Nd–Pb isotopic composition of the Harrat Al-Madinah volcanic field, Saudi Arabia. *Gondwana Res.* **21**, 670–689 (2012).
40. Rooney, T. O., Nelson, W. R., Dosso, L., Furman, T. & Hanan, B. The role of continental lithosphere metasomes in the production of HIMU-like magmatism on the northeast African and Arabian plates. *Geology* **42**, 419–422 (2014).
41. Chazot, G. & Bertrand, H. Mantle sources and magma-continental crust interactions during early Red Sea-Gulf of Aden rifting in southern Yemen: Elemental and Sr, Nd, Pb isotope evidence. *J. Geophys. Res.* **98**, 1819–1835 (1993).
42. Baker, J. A. et al. Resolving crustal and mantle contributions to continental flood volcanism, Yemen; constraints from mineral oxygen isotope data. *J. Petrol.* **41**, 1805–1820 (2000).
43. Rooney, T. O., Bastow, I. D. & Keir, D. Insights into extensional processes during magma assisted rifting: evidence from aligned scoria cones and maars. *J. Volcanol. Geotherm. Res.* **201**, 83–96 (2011).
44. De Paolo, D. J. Trace element and isotopic effects of combined wallrock assimilation and fractional crystallization. *Earth Planet. Sci. Lett.* **53**, 189–202 (1981).
45. Hegner, E. & Pallister, J. S. Pb, Sr, and Nd isotopic characteristics of Tertiary Red Sea rift volcanics from the central Saudi Arabian Coastal Plain. *J. Geophys. Res.* **94**, 7749–7755 (1989).
46. Augustin, N., Van Der Zwan, F. M., Devey, C. W. & Brandsdottir, B. 13 million years of seafloor spreading throughout the Red Sea Basin. *Nat. Commun.* **12**, 2427 (2021).
47. Okwokwo, O. I., Mitchell, N. C., Shi, W., Stewart, I. C. & Izzeldin, A. Y. How have thick evaporites affected early seafloor spreading magnetic anomalies in the Central Red Sea?. *Geophys. J. Int.* **229**, 1550–1566 (2022).
48. Delaunay, A. et al. Structure and morphology of the Red Sea, from the mid-ocean ridge to the ocean-continent boundary. *Tectonophysics* **849**, 229728 (2023).
49. Le Magoarou, C. et al. Integration of gravity, magnetic, and seismic data for subsalt modeling in the Northern Red Sea. *Interpretation* **9**, T507–T521 (2021).
50. Ali, M. et al. The Red Sea rifting in central Egypt: constraints from the offshore Quseir. *J. Geol. Soc.* **180**, jgs2022–jgs2105 (2023).

51. Issachar, R., Gómez-García, ÁM. & Ebbing, J. Lithospheric structure of the Red Sea based on 3D density modeling: A contrasting rift architecture. *J. Geophy. Res.* **128**, e2022JB025458 (2023).
52. Girdler, R. W. & Styles, P. Two stage Red Sea floor spreading. *Nature* **247**, l–11 (1974).
53. Almalki, K. A., Betts, P. & Ailleres, L. Episodic sea-floor spreading in the Southern Red Sea. *Tectonophysics* **617**, 140–149 (2014).
54. Coleman, R. G., DeBari, S. & Peterman, Z. A-type granite and the Red Sea Opening. *Tectonophysics* **204**, 27–40 (1992).
55. Yao, Z., Mooney, W. D., Zahran, H. M. & Youssef, S. E. H. Upper mantle velocity structure beneath the Arabian shield from Rayleigh surface wave tomography and its implications. *J. Geophys. Res. Solid Earth* **122**, 6552–6568 (2017).
56. Mukhopadhyay, M., Mukhopadhyay, B., Mogren, S. & Ibrahim, E. High velocity lower crust with anomalous rheological parameters under the Red Sea Passive Margin, SW Saudi Arabia—nsight into the evolution of the Hijaz-Asir Escarpment Zone. *Geophys. J. Int.* **236**, 711–726 (2024).
57. Chang, S.-J., Lim, J.-A., Mai, M. The effects of mantle plumes on the Red Sea rifting and Cenozoic volcanism in the Arabian plate. in: *Rifting and Sediments in the Red Sea and Arabian Gulf Regions* (eds Rasul N. M. A. & Stewart, I. C. F.) pp 95–105 (CRC Press, Taylor & Francis Group, Abingdon, UK, 2024).
58. Cochran, J. R. A model for the development of the Red Sea. *AAPG Bull.* **67**, 41–69 (1983).
59. Steckler, M. S. Uplift and extension at the Gulf of Suez: indications of induced mantle convection. *Nature* **317**, 135–139 (1985).
60. Reilinger, R., McClusky, S., ArRajehi, A. Geodetic constraints on the geodynamic evolution of the Red sea. in: *The Red Sea: the formation, morphology, oceanography and environment of a young ocean basin* (eds Rasul N. M. A. & Stewart, I. C. F.) pp 135–149 (Springer, Earth System Sciences, Berlin Heidelberg, 2015).
61. Oelkers, E. H. et al. The subsurface carbonation potential of basaltic rocks from the Jizan region of Southwest Saudi Arabia. *Int. J. Greenh. Gas Control* **120**, 103772 (2022).
62. Ogg, J. G. Geomagnetic Polarity Time Scale. in: "Geologic time scale 2020" (eds Gradstein, F. M., Ogg, J. G., Schmitz, M. D., Ogg, G. M.), 159–192 (Elsevier, 2020).
63. Thybo, H. & Nielsen, C. A. Magma-compensated crustal thinning in continental rift zones. *Nature* **457**, 873–876 (2009).
64. Mackenzie, G. D., Thybo, H. & Maguire, P. K. H. Crustal velocity structure across the Main Ethiopian Rift: results from two-dimensional wide-angle seismic modelling. *Geophys. J. Int.* **162**, 994–100 (2005).
65. La Rosa, A. et al. Simultaneous rift-scale inflation of a deep crustal sill network in Afar, East Africa. *Nat. Commun.* **15**, 4287 (2024).
66. Drury, S. A., Kelley, S. P., Berhe, S. M., Collier, R. E. L. & Abraha, M. Structures related to Red Sea evolution in northern Eritrea. *Tectonics* **13**, 1371–1380 (1994).
67. Kenea, N., Ebinger, C. & Rex, D. Late Oligocene volcanism and extension in the southern Red Sea Hills, Sudan. *J. Geol. Soc.* **158**, 285–294 (2001).
68. Huismans, R. & Beaumont, C. Depth-dependent extension, two-stage breakup and cratonic underplating at rifted margins. *Nature* **473**, 74–78 (2011).
69. Brune, S. et al. Geodynamics of continental rift initiation and evolution. *Nat. Rev. Earth Environ.* **4**, 235–253 (2023).
70. Daniels, K. A., Bastow, I. D., Keir, D., Sparks, R. S. J. & Menard, T. Thermal models of dyke intrusion during the development of continent-ocean transition. *Earth Planet. Sci. Lett.* **285**, 145–153 (2014).
71. Brune, S., Heine, C., Pérez-Gussinyé, M. & Sobolev, S. V. Rift migration explains continental margin asymmetry and crustal hyper-extension. *Nat. Commun.* **5**, 4014 (2014).
72. Liao, J. & Gerya, T. From continental rifting to seafloor spreading: insight from 3D thermo-mechanical modeling. *Gondwana Res.* **28**, 1329–1343 (2015).
73. Bastow, I. D. & Keir, D. The protracted development of the continent-ocean transition in Afar. *Nat. Geosci.* **4**, 248–250 (2011).
74. White, R. S., Smith, L. K., Roberts, A. W., Christie, P. A. F. & Kusznir, N. J. Lower-crustal intrusion on the North Atlantic continental margin. *Nature* **452**, 460–465 (2008). and the rest of the iSIMM Team.
75. Renne, P. R., Balco, G., Ludwig, K. R., Mundil, R. & Min, K. Response to the comment by W.H. Schwarz et al. on " Joint determination of ^{40}K decay constants and ^{40}Ar*/^{40}K for the Fish Canyon sanidine standard, and improved accuracy for ^{40}Ar/^{39}Ar geochronology" by P.R. Renne et al. (2010). *Geochim. Cosmochim. Acta* **75**, 5097–5100 (2011).
76. Lee, J.-Y. et al. A redetermination of the isotopic abundances of atmospheric Ar. *Geochim. Cosmochim. Acta* **70**, 4507–4512 (2006).
77. Koppers, A. A. P. ArAr CALC software for ^{40}Ar/^{39}Ar age calculations. *Comput. Geosci.* **28**, 605–619 (2002).
78. Schaen, A. J. et al. Interpreting and reporting ^{40}Ar/^{39}Ar geochronologic data. *Bull. Geol. Soc. Am.* **133**, 461–487 (2021).
79. Hall, C. M., Walter, R. C., Westgate, J. A. & York, D. Geochronology, stratigraphy and geochemistry of cindery tufts in Pliocene hominid-bearing sediments of the Middle Awash, Ethiopia. *Nature* **308**, 26–31 (1984).
80. Mercer, C. M. & Hodges, K. V. ArAR - A software tool to promote the robust comparison of K-Ar and 40Ar/39Ar dates published using different decay, isotopic and monitor-age parameters. *Chem. Geol.* **440**, 148–163 (2016).
81. Kuiper, K. F. et al. Synchronizing rock clocks of Earth history. *Science* **320**, 500–504 (2008).
82. Avanzinelli, R. et al. High precision Sr, Nd, and Pb isotopic analyses using the new generation Thermal Ionisation Mass Spectrometer ThermoFinnigan Triton- Ti®. *Period. Mineral.* **74**, 147–166 (2005).
83. Weis, D. et al. High- precision isotopic characterization of USGS reference materials by TIMS and MC-ICP- MS. *Geochem. Geophys. Geosyst.* **7**, Q08006 (2006).
84. Jochum, K. P. et al. GeoReM: A New Geochemical Database for Reference Materials and Isotopic Standards. *Geostand. Geoanal. Res.* **29**, 333–338 (2005).
85. Farr, T. G. & Kobrick, M. Shuttle radar topography mission produces a wealth of data. *Eos Trans. AGU* **81**, 583–585 (2000).
86. Fairer, G. M. Geologic Map of the Wadi Baysh quadrangle, Sheet 17F, Kingdom of Saudi Arabia. *Min. Pet. Miner. Resour. Deputy Minist. Miner. Resour* (1985).
87. Ligi, M. & Bortoluzzi, G. PLOTMAP: Geophysical and geological applications of good standard quality cartographic software. *Comput. Geosci.* **15**, 519–585 (1989).
88. Anders, E. & Ehibara, M. Solar-system abundances of the elements. *Geochim. Cosmochim. Acta* **46**, 2363–2380 (1982).
89. Godard, M. et al. Geochemistry of a long in-situ section of intrusive slow-spread oceanic lithosphere: Results from IODP Site U1309 (Atlantis Massif, 30°N Mid-Atlantic-Ridge). *Earth Planet. Sci. Lett.* **279**, 110–122 (2009).
90. Haase, K. M., Muhe, R. & Stoffers, P. Magmatism during extension of the lithosphere: geochemical constraints from lavas of the Shaban Deep, northern Red Sea. *Chem. Geol.* **166**, 225–239 (2000).

Acknowledgements

Work supported by the Consiglio Nazionale Ricerche and the University of Pavia. Fieldwork was the result of a joint effort of the Saudi Geological

Survey (SGS) and the Istituto di Scienze Marine, CNR of Bologna (ISMAR-CNR). We thank Dr. Z.A. Nawab, former SGS President and Dr. A.M. Alattas, former SGS Assistant President for Technical Affairs. We thank the Istituto di Geologia Ambientale e Geoingegneria (Dr. M. Moscatelli) for contributing to the processing costs of the article. The research was sponsored by the Progetti di Rilevante Interesse Nazionale Funding Program (PRIN_2017KY5ZX8 and PRIN_2022PC9NME).

Author contributions

M.L. and A.S. wrote the initial paper and, along with L.V. and N.R., designed the study and conducted the fieldwork. R.A., V.B., A.B., and S.C. performed the geochemical and isotopic analyses, H.G. and S.N. carried out the Ar/Ar dating, and A.D. contributed to the interpretation of the results. All authors discussed the results, provided feedback, and contributed to the final paper.

Competing interests

The authors declare no competing interests.

Additional information

Supplementary information The online version contains supplementary material available at https://doi.org/10.1038/s41467-025-61598-0.

Correspondence and requests for materials should be addressed to Marco Ligi.

Peer review information *Nature Communications* thanks Shelby Bowden, and the other, anonymous, reviewer(s) for their contribution to the peer review of this work. A peer review file is available.